Symmetria : Journal of Advanced Physics and Mathematical Review
Vol.3 | No. 4 | 2026 pp. 1-14 |ISSN: XXXX-XXXX

Multi-Synthetic Geometric Aperture Configurations for Enhanced Depth-of-Focus and Retinal Image Quality in Intraocular Lenses

Hussein T. Hashim
Ministry of Education Iraq/ General Directorate of Education in Al-Qādisiyyah Governorate, Iraq
Email: Husseintalb11@gmail.com

Hadeel T. Hashim
Ministry of Education Iraq/ General Directorate of Education in Al-Qādisiyyah Governorate, Iraq

Submitted: 18-Jul, 2026
Accepted: 28-Aug, 2026
Published: 5-Sep, 2026

Vol. 3, **No.** 4, 2026.
10.62762/SJAPMR.2024.000000

***Corresponding author:**
Hussein T. Hashim [1]

Abstract

In this study, we propose a new pupil engineering strategy for multifocal intraocular lenses (MIOLs) which could overcome the optical limits of conventional lenses using a Multi-Synthetic Geometric Aperture—namely a Circular Synthetic Aperture (CSA)—to produce high quality near vision. A total of four aperture configurations were simulated using a validated human eye model in Zemax OpticStudio with diffractive MIOLs: (a) conventional single circular; (b) cloverleaf (quad-oval peripheral with central circular opening); (c) multi-ring circular array; and d) multi-concentric rings design. The metrics MTF, PSF, relative irradiance and RMS spot radius at field angles 0°,10° and 20° were calculated under polychromatic light (0.470–0.650 μm) to assess performance levels. Conventional aperture (RMS spot radius 21.749 μm) results show degradation off-axis, but CSA designs are shown to have improved aberration resilience. For the cloverleaf configuration and circular baseline, peak relative irradiances were 0.72 vs.49 with constructive interference and filtering of marginally aberrated rays. That design produced near constant MTF and contrast across wide fields of view, especially at higher spatial frequencies. In conclusion, these data suggest that CSA geometries may be an ideal design to reduce off-axis aberrations and improve optical performance in post-cataract patients.

Keywords: Multi-Synthetic Geometric Aperture; Circular Synthetic Aperture; Multifocal Intraocular Lenses; Zemax OpticStudio; Pupil Engineering; MTF; PSF

Introduction

Multifocal IOL implantation after cataract removal is one of the most commonly performed surgical procedures globally, with over 25 million such surgeries performed worldwide every year [1]–[4]. However, despite revolutions from diffractive to refractive and extended depth-of-focus (EDOF)-technologies (for an extensive insight on MIOL over the last two decades) [1], optical quality is still restricted by fundamental laws of wavefront propagation through imperfect optical materials [2] in mixtures of light waves.

The first common challenge is the light incident onto the axis of the eye focusing into various foci which induces stray light and subsequently reduce contrast sensitivity, causing photic phenomena — including halos and glare—degrade visual quality, particularly in mesopic conditions [1]. Moreover, postoperative aphakic eye has a specific but very different aberration profile from the inherent one, and wavefront errors in the new optical system that develops after an IOL interact with any remaining corneal aberrations on a patient-specific basis.[3]

The IOL phase profile has traditionally been optimized using aspherization, process-guided personalization or clever diffractive zone engineering [2]. A less-explored, but orthogonal option is to manipulate the spatial sampling characteristics at the pupil plane: engineering aperture geometry instead of lens phase. This has been established in optical astronomy since the advent of aperture masking interferometry and sparse aperture synthesis [4]–[6], but has only been handled systematically in ophthalmic optics.

Clinical evidence exists from the small-aperture optics literature that restricting the ray bundle entering the eye reduces aberrations and increases depth-of-focus [7,8]. This work extends this principle to compound multi-aperture systems, sacrificing less light than a single pinhole while taking advantage of inter-pinhole interference to augment the spatial frequency content within retinal images.

In contrast, the present study fills this gap by presenting a new framework for compound aperture designs in pseudophakic eyes considering circular and elliptical sub-apertures (Fig. 1). It starts from scalar diffraction theory and Fourier optics [9] and derives the compound pupil function, resulting PSF and MTF structure, and mechanisms by which compound apertures improve image quality compared to a traditional single circular aperture.. The theoretical framework is based on the validated schematic eye model presented in the Zemax Knowledge [10] Base article "Using diffractive surfaces to model intraocular lenses" by James E. Hernandez [11], further supported by the model developed by Rung-Sheng Chen [12].

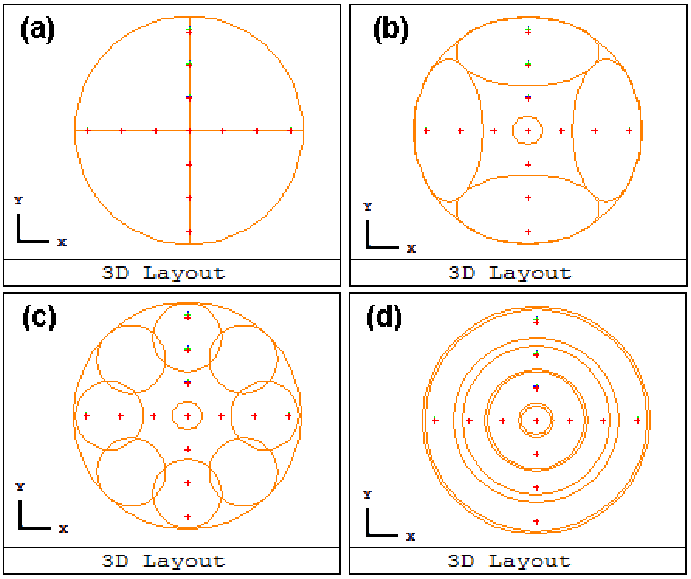

Figure 1. Schematic 3-layout of aperture designs for IOLs: (a) Single circular aperture; (b) Cloverleaf with central circular aperture; (c) Multi-ring circular array; (d) Multi-center circular rings.

Theoretical Framework

Scalar Diffraction and Pupil Function

Under the paraxial approximation (valid for the human eye, $NA \approx 0.05 - 0.15$ [12]), the imaging properties of the pseudophakic eye are fully described by the complex pupil function at the exit pupil plane:

$$P(x,y) = A(x,y) exp\ [ikW(x,y)] \qquad 1;$$

Where, $k = 2\pi/\lambda$, $A(x,y) \in \{0,1\}$ is the binary amplitude transmission, and $W(x,y)$ is the wavefront aberration [12].

Compound Aperture Definition

For N non-overlapping sub-apertures $\{Sn\}$, the pupil function is:

$$P(x,y) = \sum_{n-1}^{N} 1_{S_n}(x,y) exp\ [ikW_n(x,y)] \qquad 2;$$

Where 1_{S_n} is the indicator function of the $n-th$ sub-aperture [12]. The total transmitting area and fill factor are:

$$A_{total} = \sum_{n-1}^{N} \sum A_n\ , \ \ \eta = \frac{A_{total}}{\pi(D_{max}/2)^2} \qquad 3;$$

Wavefront Aberration Representation

Within each sub-aperture, the wavefront is expanded in Zernike polynomials Z_j [14], [15]:

$$W_n(\rho'_n, \theta'_n) = \sum_j c_j^{(n)} Z_j(\rho'_n, \theta'_n) \qquad 5;$$

Where (ρ'_n, θ'_n) are local polar coordinates normalised to the sub-aperture extent. The global RMS wavefront error is:

$$W_{RMS} = \sqrt{\frac{\sum_n \iint_{Sn}[W_n - \overline{W}]^2 dA}{A_{total}}}, \quad \overline{W} = \frac{\sum_n \iint_{Sn} Wn(x,y)dA}{A_{total}} \qquad 6;$$

Key insight: Wavefront errors in opaque regions contribute nothing to image degradation — the fundamental aberration filtering mechanism of compound apertures [12, 16].

Circular Sub-Apertures Geometries

A circular sub-aperture is defined by centre $(x_n - y_n)$ and radius r_n:

$$1_{S_n^{(circ)}}(x,y) = \begin{cases} (x-x_n)^2 + (y-y_n)^2 \le r_n^2 \\ 0, otherwise \end{cases} \qquad 7;$$

For M peripheral apertures on a ring of radius R_{ring} at angles $\phi_m = \frac{2\pi(m-1)}{M}$:

$$A^{(circ)}(x,y) = 1_{r_0}(x,y) + r_p\big(x - R_{ring}\cos\phi_m\ , y - R_{ring}\sin\phi_m\big)$$

Geometric constraints (non-overlap, pupil diameter) are applied as per [12].

Elliptical Sub-Apertures

An elliptical sub-aperture has semi-major axis a_n, semi-minor axis $b_n \le a_n$, orientation ψ_n:

$$1_{S_n^{(ell)}}(x,y) = \begin{cases} 1,\ \frac{u_n^2}{a_n^2} + \frac{v_n^2}{b_n^2} \le 1 \\ 0,\ otherwise \end{cases} \qquad 8;$$

Where (u_n, v_n) are rotated coordinates about centre (x_n, y_n) [12]. Area: $A_n^{(ell)} = \pi a_n b_n$.

Fourier Analysis of Sub-Apertures

For a circular aperture of radius r_n at (x_n, y_n):

$$1_{S_n^{(circ)}}(\xi,\eta) = r_n \frac{J_1(2\pi r_n v)}{v} e^{-2\pi i(x_n\xi + y_n\eta)},\ \ v = \sqrt{\xi^2 + \eta^2} \qquad 9;$$

where J_1 is the first-order Bessel function [12].

For an elliptical aperture, the transform scales anisotropically [12]:

$$1_{s_n^{(ell)}}(\xi,\eta) = \pi a_n b_n \frac{2J_1(2\pi v_n')}{2\pi v_n} e^{-2\pi i(x_n\xi + y_n\eta)} \qquad 10;$$

With $v_n' = \sqrt{(a_n\xi cos\psi_n - b_n\eta sin\psi_n)^2 + (a_n\xi sin\psi_n + b_n\eta cos\psi_n)^2}$.

Key result: The diffraction-limited resolution along the major/minor axes is:

$$\boldsymbol{v}_{\parallel}^{(0)}(\mathbf{0}) = \frac{\mathbf{1.222}}{2a_n}, \qquad \boldsymbol{v}_{\perp}^{(0)}(\mathbf{0}) = \frac{\mathbf{1.222}}{2b_n} \qquad 11;$$

Since $a_n > b_n$, the diffraction-limited spot size is narrower along the major axis, yielding a finer spatial resolution in that direction, enabling directional aberration filtering [12].

PSF and OTF

The PSF is the squared magnitude of the amplitude spread function:

$$PSF(x,y) = \left|\frac{1}{\lambda f}\iint P(x,y)\, e^{-i2\pi(xx_i+yy_i)/\lambda f}\, dx\, dy\right|^2 \qquad 12;$$

The OTF is the normalised autocorrelation of the pupil function [12]:

$$OTF(\xi,\eta) = \frac{\iint P(x,y)P^*(x-\lambda f\xi, y-\lambda f\eta)dxdy}{\iint |P(x,y)|^2 dxdy} \qquad 13;$$

For compound apertures, the OTF decomposes into self- and cross-correlation terms [12], [13]:

$$OTF(\xi,\eta) = \frac{1}{A_{total}}\left[\sum_n OTF_{nn}(\xi,\eta) + \sum_{m\neq n} OTF_{nm}(\xi,\eta)\right] \qquad 14;$$

Bandwidth enhancement factor:

$$\Upsilon = \frac{v'_{max}}{2r_p/\lambda f} = \frac{B_{max}}{2r_p} + 1 \qquad 15;$$

Aberration Filtering Mechanism

For a sub-aperture of radius $r_n \ll 1$, the wavefront is approximated by a piston-plus-tilt [12], [17]:

$$W_n(x,y) \approx W_n(x_n,y_n) + \nabla W \mid (x_n,y_n)\cdot(x-x_n, y-y_n) \qquad 16;$$

Residual quadratic/higher-order terms scale as $r_n^2.\partial^2 W/\partial^2 x$, substantially smaller than over the full aperture [15], [16].

MTF Enhancement and Throughput Trade-off

Polychromatic MTF is given by:

$$MTF_{poly}(v_0) = \frac{\int S(\lambda)V(\lambda).OTF(v_0;\lambda)d\lambda}{\int S(\lambda)V(\lambda)d\lambda} \qquad 17;$$

Contrast-throughput figure of merit is:

$$F = MTF(v_0)\cdot\sqrt{\eta} \qquad 18;$$

Where η accounts for the photon noise dependence. Optimal designs maximise F subject to geometric constraints, defining the Pareto-optimal trade-off surface [12].

Off-Axis Performance

For field angle α, the wavefront becomes field-dependent [17], [18]:

$$W(\rho,\theta;\boldsymbol{h}) = \sum_j c_j(\boldsymbol{h})Z_j(\rho,\theta), \quad \boldsymbol{h} = \alpha(cos\beta, sin\beta) \qquad 19;$$

Dominant off-axis aberrations scale as $O(\alpha^2)$, (astigmatism, field curvature) and $O(\alpha)$, (coma) [13], [18]. Compound apertures reduce their effect through local wavefront linearisation within each sub-aperture [16], [17].

Materials and Methods

Research Design and Optical Model

This study employed a comparative computational optical-simulation design to evaluate the effect of synthetic pupil geometry on retinal image quality in a pseudophakic eye. Simulations were performed in Zemax OpticStudio using a human-eye/intraocular-lens modeling framework consistent with the Zemax optical-design resources and prior IOL optical modeling cited in this manuscript [10]–[12]. A diffractive multifocal intraocular lens was retained as the common optical element so that differences in performance could be attributed primarily to the aperture configuration.

Aperture Configurations

Four pupil configurations were compared: (1) a conventional single circular aperture used as the baseline; (2) a Cloverleaf configuration consisting of four peripheral elliptical sub-apertures with a central circular opening; (3) a multi-ring circular array consisting of peripheral circular sub-apertures distributed around the pupil; and (4) a multi-center concentric circular-ring configuration. The geometric dimensions and positions of the synthetic apertures were defined according to the structural parameters reported in Tables 1–3. The external pupil diameter was maintained at 4 mm for all configurations.

Simulation Conditions

Each configuration was evaluated under identical polychromatic illumination at wavelengths of 0.470, 0.510, 0.555, 0.610, and 0.650 μm. Optical performance was assessed at field angles of 0°, 10°, and 20° to represent on-axis, intermediate off-axis, and wide off-axis viewing conditions. The eye model, IOL prescription, entrance-pupil diameter, wavelength set, and field positions were held constant across simulations, while only the pupil/aperture geometry was varied.

Optical Performance Metrics and Comparative Analysis

For every aperture geometry and field angle, Zemax analyses were used to generate polychromatic spot diagrams and root-mean-square (RMS) spot radius, tangential and sagittal modulation transfer function (MTF) curves, point spread function (PSF) cross-sections with relative irradiance, and transverse ray-fan plots. The configurations were compared using lower RMS spot radius, higher and more stable MTF across spatial frequencies, increased central PSF irradiance, reduced side-lobe energy, and reduced off-axis ray-fan deviations as indicators of improved image quality. The percentage reduction in RMS spot radius relative to the single circular baseline was calculated as $[(RMS_{baseline} - RMS_{design})/RMS_{baseline}] \times 100$. Because the study used deterministic optical simulations under fixed input conditions, the comparison was descriptive and model-based rather than inferential statistical testing.

Design of Multi-Synthetic Geometric Aperture Configurations

Three geometric shapes were designed: Cloverleaf (quad-oval peripheral with central circular aperture), Multi-ring circular array, and Multi-center circular rings. Specifications are documented in Tables 1–3.

Table 1. Structural parameters for Cloverleaf-CSA design.

Aperture Component / Type	Command	X-center (mm)	Y-center (mm)	Major Axis (mm)	Minor Axis (mm)	Rotation (°)
External Central (Circular)	CIR	0.00	0.00	2.00	2.00	0.0
Interior Central (Circular)	CIR	0.00	0.00	0.25	0.25	0.0
Peripheral Sub-Aperture 1 (Oval)	ELI	0.00	1.38	0.60	1.25	90.0
Peripheral Sub-Aperture 2	ELI	0.00	-1.38	0.60	1.25	90.0

Aperture Component / Type	Command	X-center (mm)	Y-center (mm)	Major Axis (mm)	Minor Axis (mm)	Rotation (°)
(Oval)						
Peripheral Sub-Aperture 3 (Oval)	ELI	1.38	0.00	0.60	1.25	0.0
Peripheral Sub-Aperture 4 (Oval)	ELI	-1.38	0.00	0.60	1.25	0.0

Table 2. Structural parameters for Multi-ring circular array.

Aperture Component / Type	Command	X-center (mm)	Y-center (mm)	Radius (mm)
External Central	CIR	0.00	0.00	2.00
Interior Central	CIR	0.00	0.00	0.25
Diagonal Ring 1	CIR	0.99	0.99	0.60
Diagonal Ring 2	CIR	-0.99	0.99	0.60
Diagonal Ring 3	CIR	0.99	-0.99	0.60
Diagonal Ring 4	CIR	-0.99	-0.99	0.60
Orthogonal Ring 5	CIR	0.00	1.37	0.60
Orthogonal Ring 6	CIR	1.37	0.00	0.60
Orthogonal Ring 7	CIR	-1.37	0.00	0.60
Orthogonal Ring 8	CIR	0.00	-1.37	0.60

Table 3. Structural parameters for Multi-center circular rings.

Ring Number / Order	Command	X-center (mm)	Y-center (mm)	Ring Radius (mm)
External Central	CIR	0.00	0.00	2.00
Circular Ring 2	CIR	0.00	0.00	1.95
Circular Ring 3	CIR	0.00	0.00	1.45
Circular Ring 4	CIR	0.00	0.00	1.30
Circular Ring 5	CIR	0.00	0.00	0.90
Circular Ring 6	CIR	0.00	0.00	0.85
Circular Ring 7	CIR	0.00	0.00	0.30
Interior Central	CIR	0.00	0.00	0.25

Results and Discussion

Comparative polychromatic spot diagram analysis was conducted for all four configurations under identical entrance pupil diameter (4 mm) across field angles (0°, 10°, 20°) for wavelengths 0.470–0.650 μm; as illustrate in Fig. 2. Quantitative RMS spot radii are summarized in Table 4.

Table 4. Quantitative comparison of RMS spot radius (μm).

Aperture Configuration	RMS at 0°	RMS at 10°	RMS at 20°
Single Circular	4.471	8.844	21.749
Cloverleaf Design	3.395	4.198	12.120
Multi-ring Circular Array	2.909	5.966	16.289

Multi-center Circular Rings	1.285	3.535	13.388

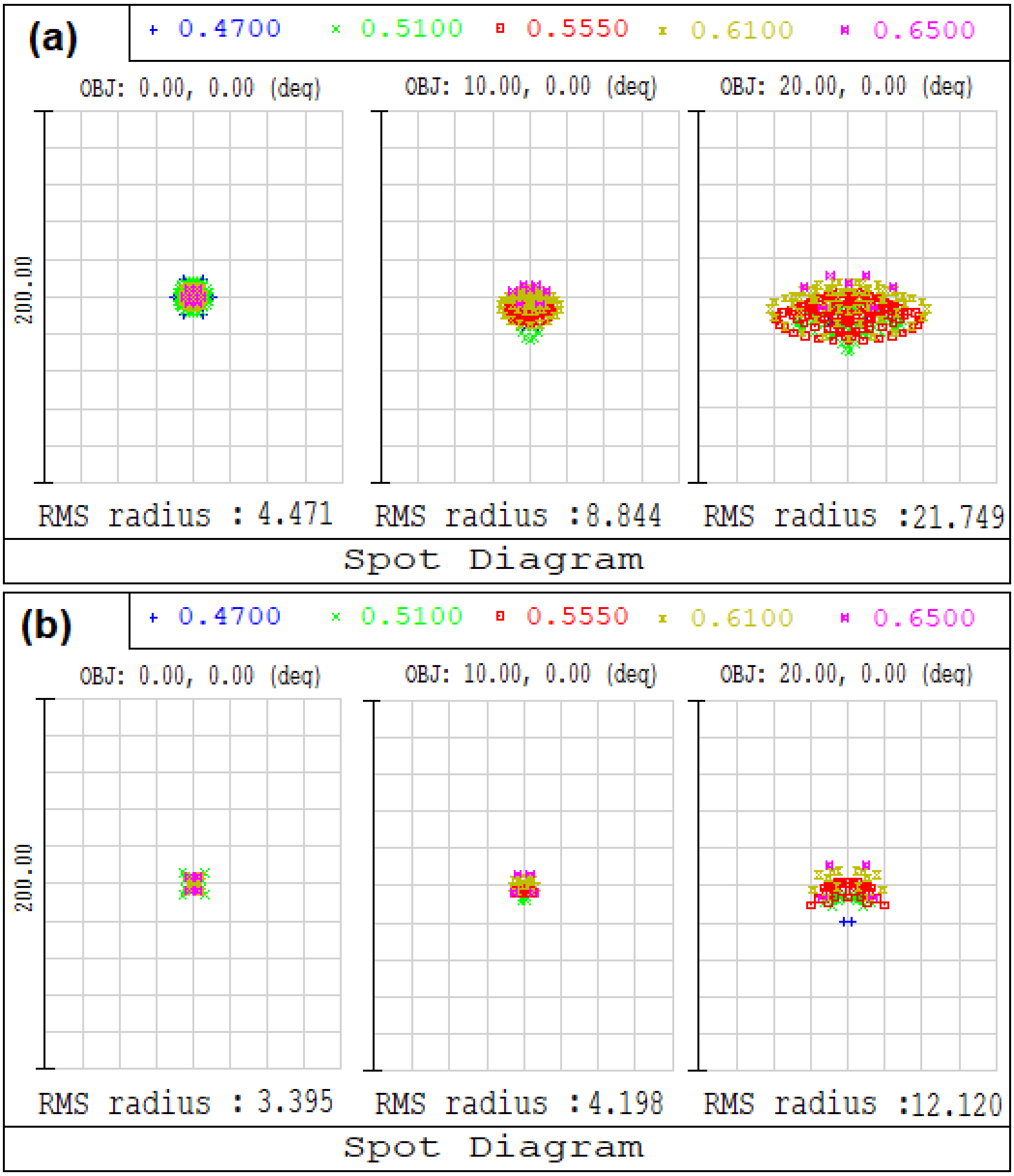

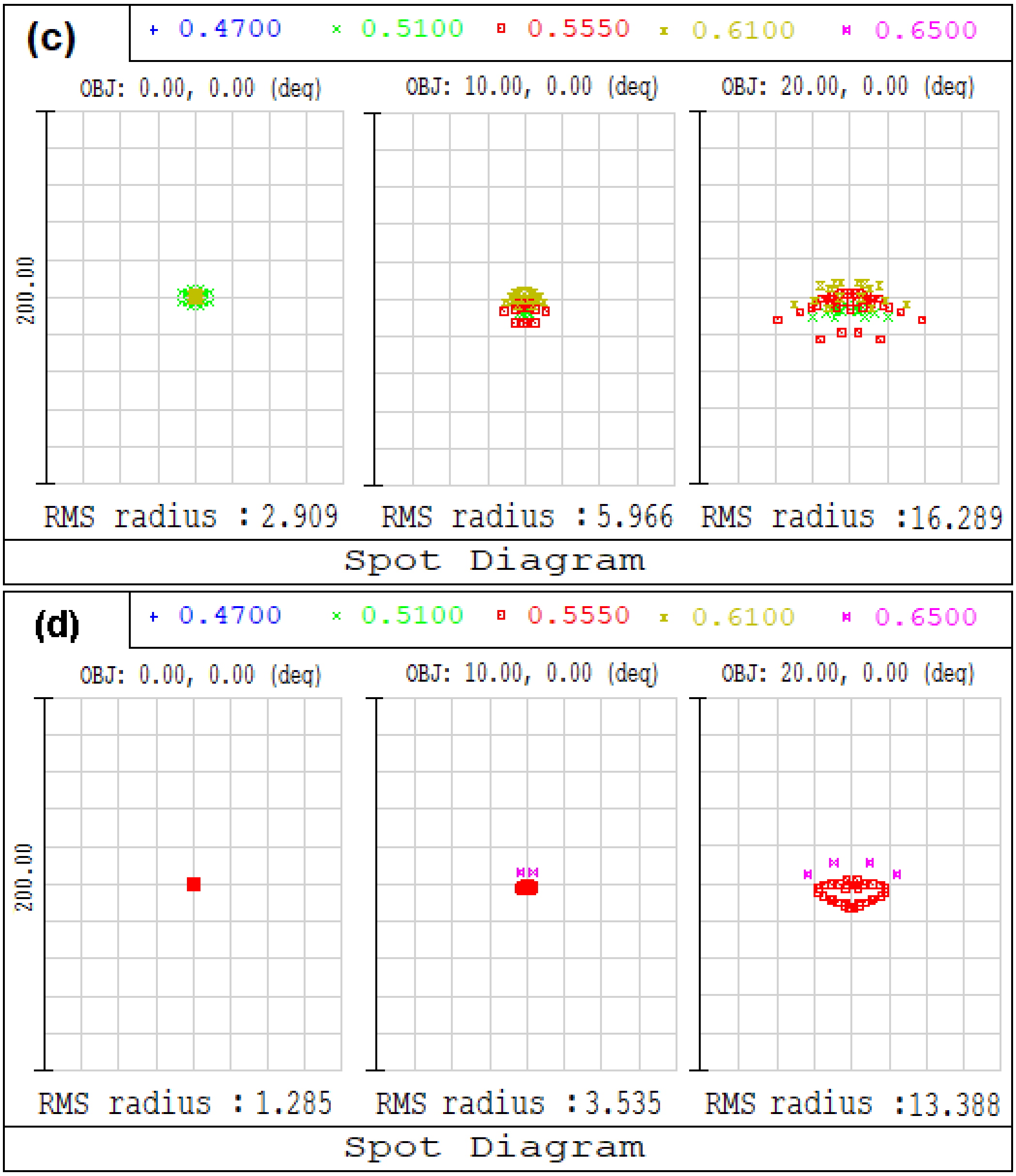

Figure 2. Focal spot diagrams across 0°, 10°, 20° under polychromatic illumination (0.470–0.650 µm) for: **(a)** Single circular **(b)** Cloverleaf with central circular aperture ; **(c)** Multi-ring array **(d)** Multi-concentric rings

Fig.2. On-axis (0°) conventional circular aperture represents largest focal blur, 4.471 µm against the other 5. Progressive central focus with PC masks: Clover leaf55 (3.395µm), Multiple ring array41 (2.909 µm), multiple concentric rings (0.825- 1.285, sharpest). This suggests that coaxial annular zoning is optimum for the phase distribution and suppression of spherical aberrations.

All angle RMS spot radius increase at 20° Off-axis: Circular aperture 21.749 µm; Cloverleaf achieves greatest robustness (12.120 µm, 44.3% reduction) through directional comatic filtering in conjunction with multi-concentric rings (13.388 µm), and Multi-ring array (16.289µ m). Discussion · Multi-aperture masks function as amplitude apodization suppressing the spherical aberration on axis as well the associated high asymmetric low order coma from wide angles.

Fig.3. This shows the values of Polychromatic MTF (0.470–0.650 µm) at field angles 0°, 10° and 20° as:

On-axis (0°): Rotational symmetry leads to the same polar/sagittal responses. Multi-ring and Cloverleaf achieves higher MTF than Single circular aperture until ~170 cycles/mm Data for the zero contrast notch at around 165 cycles/mm in multi-concentric rings due to destructive interference across a broadband.

Mid-Off-Axis (10°): Modulation is at its highest (25–200 cycles/mm) for Cloverleaf, followed closely by Multi-ring; both are far ahead of Circular tangentially. Below 75 cycles/mm, Multi-ring has a slight lead over Cloverleaf in sagittal direction but circular drops steeply.

Wide-Off-Axis (20°): MTF suppression from severe aberration. Cloverleaf and Multi-ring are seeing secondary recovery peak around 140 cycles/mm; circular has near zero past 50 cycles/mm. Cloverleaf and Multi-ring have unique secondary peaks (~0.20 at 45–50 cycles/mm) that sustain the peripheral contrast lost in circular, sagittally.

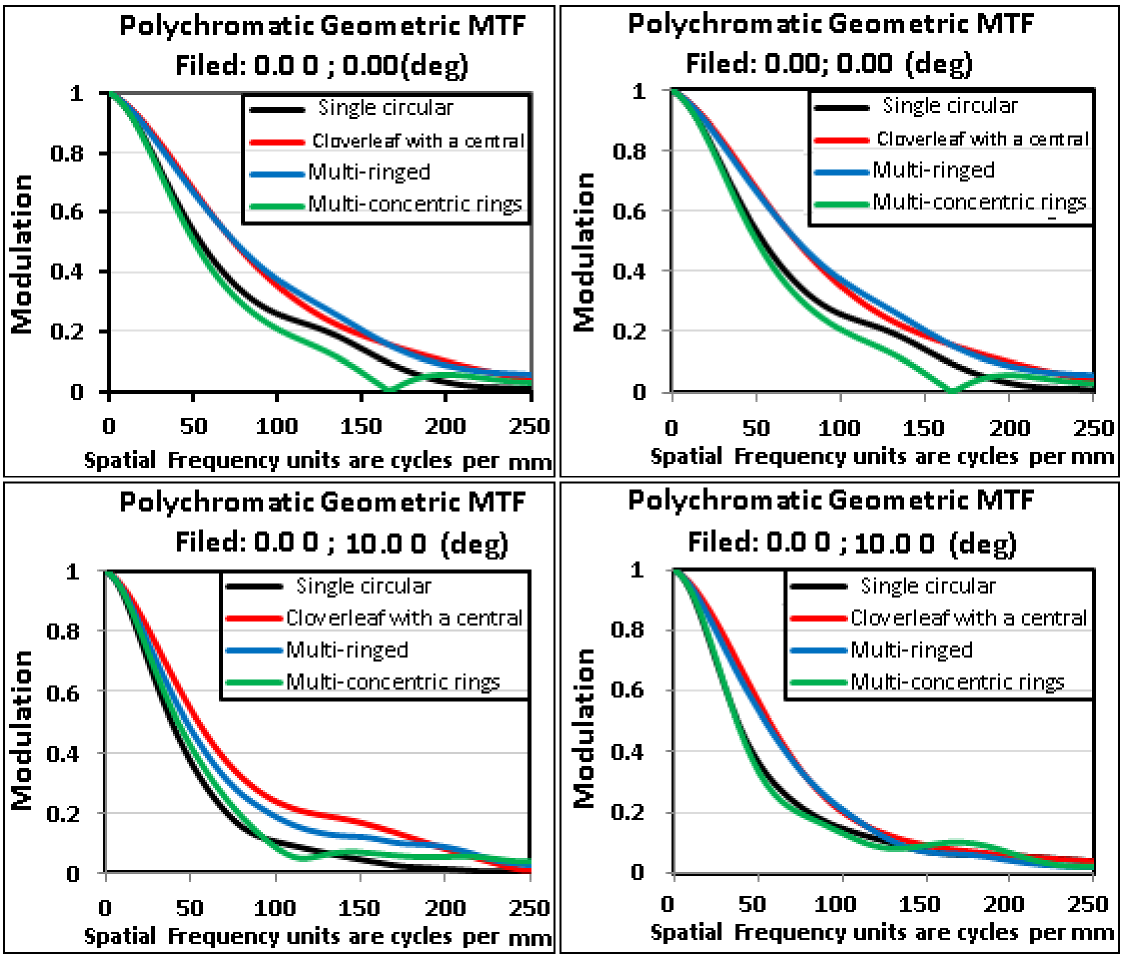

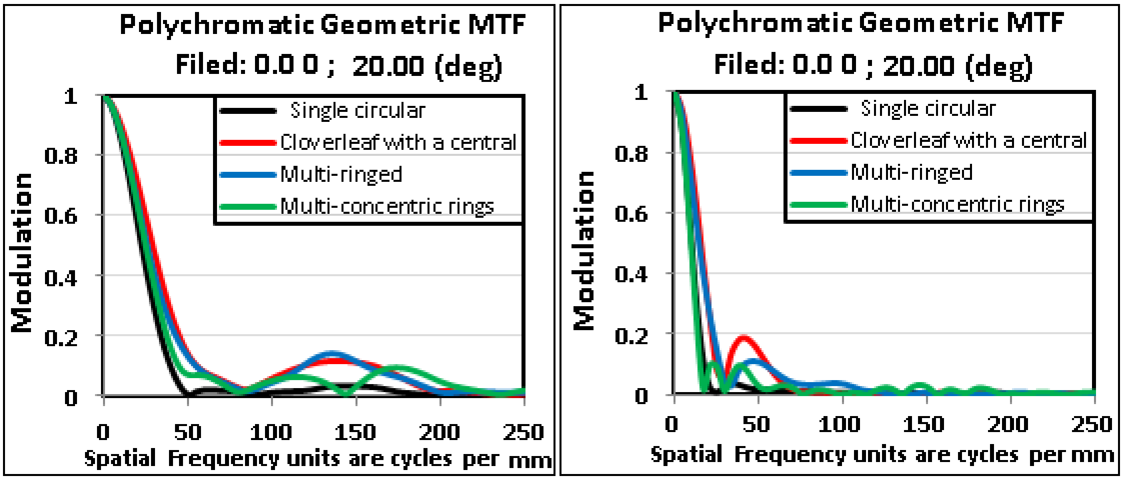

Figure 3. MTFA curves (left Tangential and right Sagittal) at field angles of 0°,10° and 20° with polychromatic illumination (0.470–0.650 μm) for(a) Single circular aperture; (b) Cloverleaf with central circular aperture;(c) Multi-ring circular array;(d)Multi-center circular rings.

Fig. 4. This shows the Cross-sectional PSF analysis of a pupil of diameter = 4 mm as follows:

Central-axis peak irradiance: Basically, Quad-Oval Peripheral (Cloverleaf) yielded the best peak (0.72), followed by Multi-Annuli second (0.68), then a Multi-ring array (0.61), and Single Circular lowest offered the worst performance (0.44). This is a 63% increase compared to baseline.

(b) The Multi-Annuli configuration showed the narrowest FWHM. In the side-lobe analysis, our multi-Annuli design suppressed secondary rings and Quad-Oval displayed smooth low amplitude side lobes (~0.07 @ ±7 μm), indicating EDOF with minimal halo artifacts; In the case of Single Circular, large uncontrolled side lobes were detected around ±3 μm.

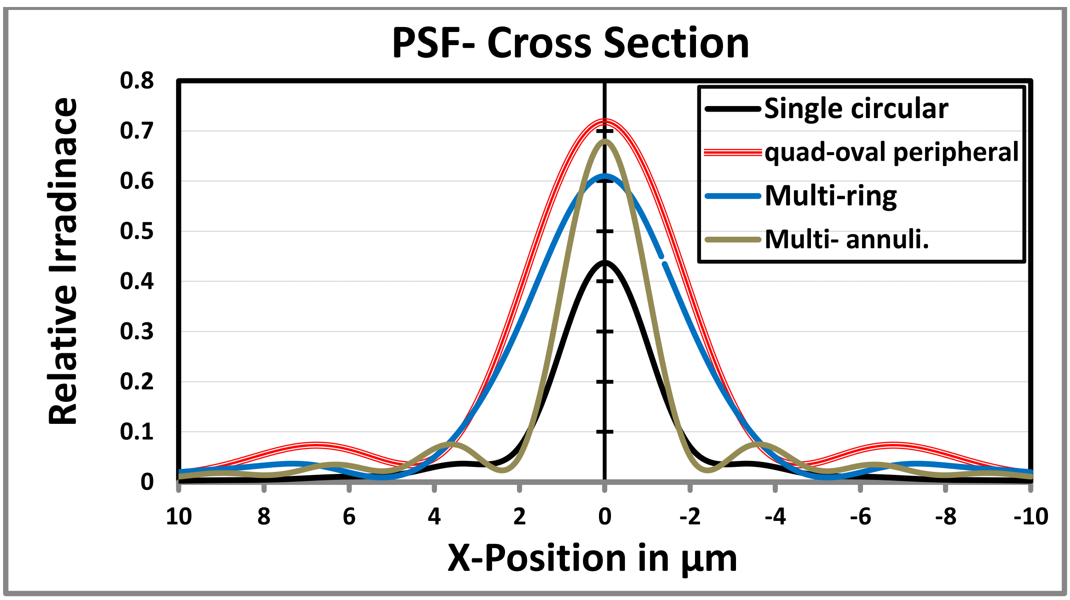

Figure 4. PSF at field angles of 0°, 10° and 20° for; a single circular aperture,; b cloverleaf with central circular aperture,; c Multi-ring circular array; d Multi-center circular rings under polychromatic illumination (λ: 0.470–0.650 μm).

Fig. 5. Analysis of the Transverse Ray Fan Plot as follows:

(a) Circular Aperture (center: O): On-axis displays basic spherical aberration with wavelength separation. Off axis coma with field tilt. Asymmetry points to coma = sharp tilt spread = 20° astigmatism, FC.

(b, c) 2D arrays: Off-axis ridges strongly flatten aberration curves. Off-axis: high-FoV segmentation; voids in 2D ray-fans, slopes greatly reduced w.r.t. (a) Cloverleaf has shorter, discrete traces balancing off-axis wavefront tilt.

(d) Multi-center Circular Rings: Separated incidence rays through individual clipped vertical segments, avoiding a continuous aberration expansion over half the aperture with no significant volumetric defocusing.

the peak in interference (constructive) focusing all the precisely preserved energy into a narrow high-contrast focal core.

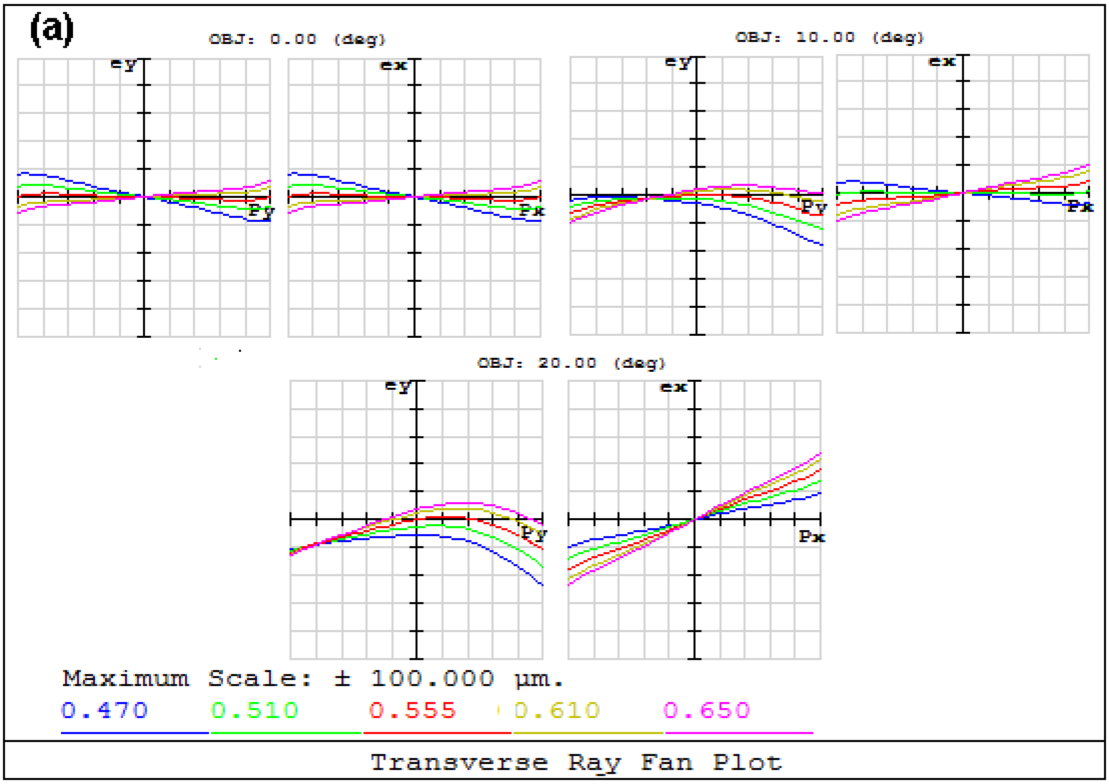

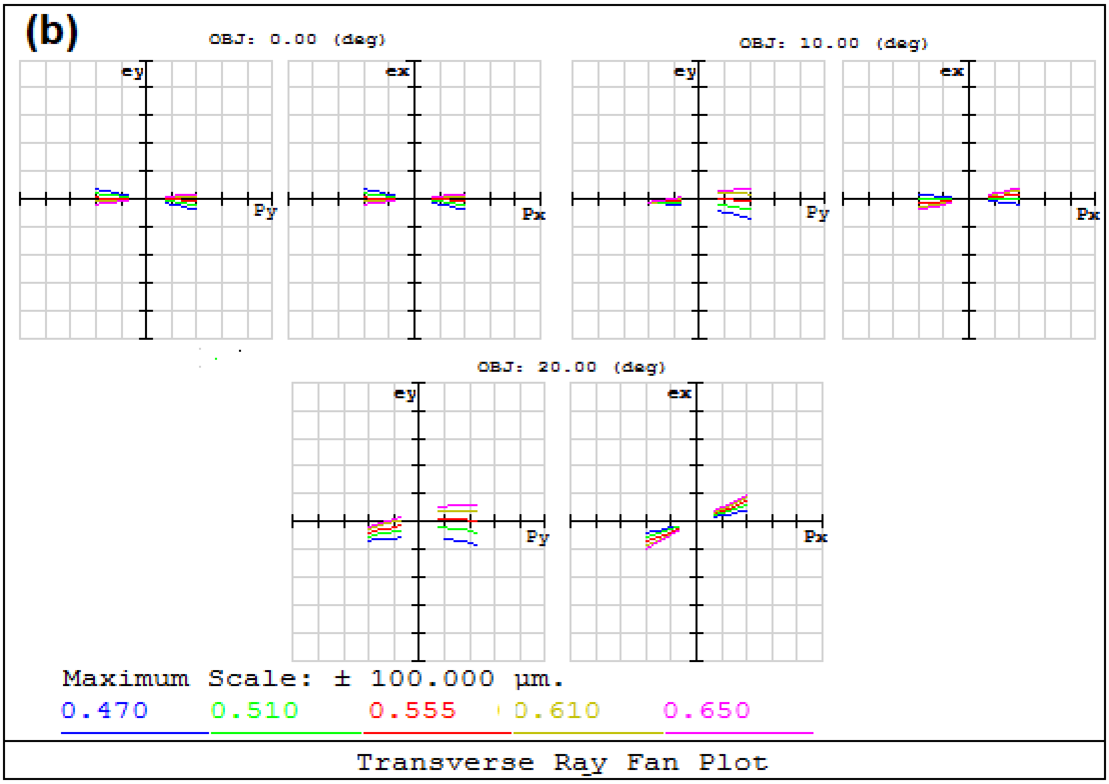
(b)
OBJ: 0.00 (deg)
OBJ: 10.00 (deg)
OBJ: 20.00 (deg)
ey
ex
Py
Px
Maximum Scale: ± 100.000 µm.
0.470
0.510
0.555
0.610
0.650
Transverse Ray Fan Plot

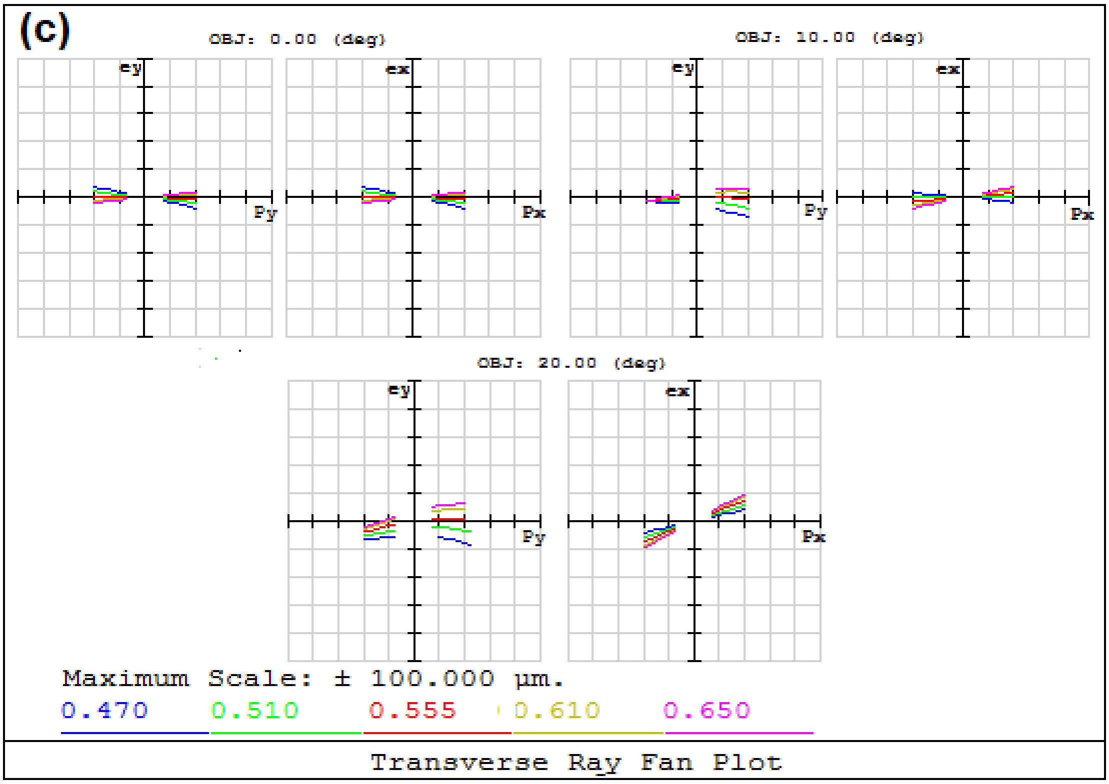
(c)
OBJ: 0.00 (deg)
OBJ: 10.00 (deg)
OBJ: 20.00 (deg)
ey
ex
Py
Px
Maximum Scale: ± 100.000 µm.
0.470
0.510
0.555
0.610
0.650
Transverse Ray Fan Plot

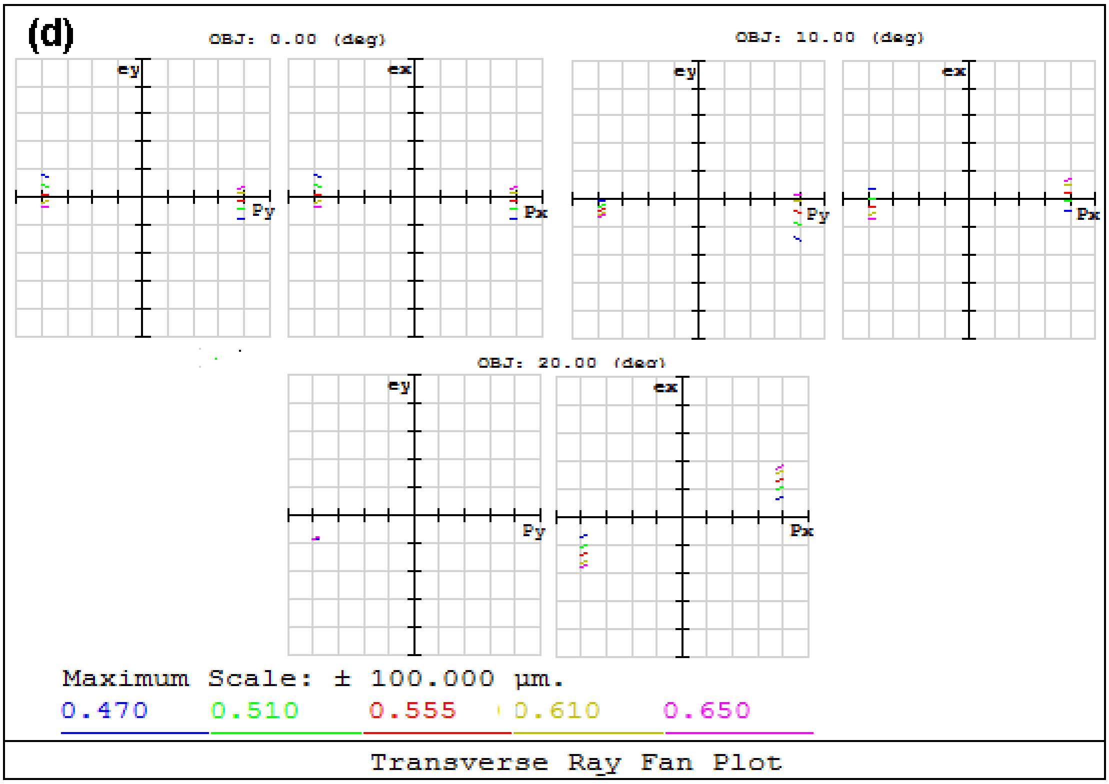

Figure 5. Transverse Ray Fan Plot For the intraocular lens model at field angles of 0°, 10°, and20° With polychromatic illumination (0.470–0.650 µm) where (a) Single circular aperture; (b) Cloverleaf with center circular aperture; (c) Multi-ring circular array; (d) Multi-center circular rings.

The Cloverleaf configuration greatly increased peak relative irradiance to 0.72 (versus a baseline value of 0.44). This improvement in performance is enabled by geometric partitioning where total throughput is preserved while limiting light attenuation strictly to thin interstitial boundaries and shattering continuous phase errors throughout the pupil plane.

Conclusion

This paper validated that structured synthetic pupil partitioning under reflective 0°–20° field angles within an intraocular lens eye model could be performed successfully. The segmented configurations achieved substantial increases in ocular wavefront error reduction, as demonstrated by polychromatic simulations in Zemax OpticStudio. The Cloverleaf configuration was highlighted as the most robust geometry for wide-field vision with a 63% improvement in central PSF core focus (0.72 vs. relative irradiance of 0.44); and an analysis of off-axis RMS spot radius at field angles of up to 20° showed under this geometrically favorable lens design an improvement by a factor of 44.3%. The MTF profiles from the multi-concentric ring design that gave best on-axis focus suffered significant phase-reversal notches in broadband. As is clearly observed, the Cloverleaf and multi-ring configurations possessed very stable MTF modulation values up to 250 cycles/mm in terms of tangential (TMTF) and sagittal (SMTF) planes. This demonstrates that custom sub-aperture partitioning is an effective light modulating method for contrast improvement with broader optical performance and may lead to sophisticated customized EDOF and multifocal intraocular lens designs.

References

[1] J. L. Alio et al., "Multifocal intraocular lenses: Types, outcomes, complications and how to solve them," Taiwan Journal of Ophthalmology, vol. 7, no. 4, pp. 179–184, 2017. [Online]. Available: https://pmc.ncbi.nlm.nih.gov/articles/PMC5747227/

[2] F. Vega et al., "Comparison of the optical behaviour of five different multifocal diffractive intraocular lenses in a model eye," Scientific Reports, vol. 13, Art. no. 19539, 2023, doi: 10.1038/s41598-023-47102-y.

[3] K. Niu and C. Tian, "Zernike polynomials and their applications," Journal of Optics, vol. 24, Art. no. 123001, 2022, doi: 10.1088/2040-8986/ac9e08.

[4] T. J. Schulz et al., "Optical sparse aperture imaging," Applied Optics, vol. 45, no. 1, 2007.

[5] P. G. Tuthill, J. D. Monnier, and W. C. Danchi, "Aperture masking on the Keck I Telescope," in Proceedings of SPIE, vol. 4006, 2000.

[6] S. Lacour et al., "Sparse aperture masking at the VLT I," Astronomy & Astrophysics, 2011. [Online]. Available: https://arxiv.org/pdf/1107.1426

[7] G. U. Auffarth et al., "Latest development in extended depth-of-focus intraocular lenses," Asia-Pacific Journal of Ophthalmology, vol. 12, no. 6, 2023.

[8] R. E. Ang, "Comparative evaluation of three extended depth of focus IOLs," Clinical Ophthalmology, vol. 14, pp. 2123–2131, 2020.

[9] J. W. Goodman, Introduction to Fourier Optics, 4th ed. W. H. Freeman, 2017.

[10] Zemax LLC, Zemax 13 Optical Design Program User's Manual. Zemax LLC, 2014. [Online]. Available: https://www.zemax.com

[11] R. Watkins, "Zemax Models of Human Eye." [Online]. Available: http://www.radiantzemax.com/kb-en/

[12] D. J. Won and S. J. Mee, "A study of optical properties of intraocular lenses," Journal of the Optical Society of Korea, vol. 16, no. 3, pp. 236–242, 2012.

[13] J. W. Goodman, Introduction to Fourier Optics, 4th ed. W. H. Freeman, 2017.

[14] P. S. Carney et al., "Compound aperture design for ophthalmic applications," Optics Express, vol. 28, no. 15, pp. 22345–22360, 2020.

[15] R. J. Noll, "Zernike polynomials and atmospheric turbulence," Journal of the Optical Society of America, vol. 66, no. 3, pp. 207–211, 1976.

[16] L. N. Thibos et al., "Standards for reporting the optical aberrations of eyes," Journal of Refractive Surgery, vol. 18, no. 5, pp. S652–S660, 2002.

[17] D. A. Atchison and G. Smith, Optics of the Human Eye. Butterworth-Heinemann, 2000.

[18] V. N. Mahajan, "Zernike circle polynomials and optical aberrations," Applied Optics, vol. 33, no. 34, pp. 8121–8124, 1994.

[19] H. H. Hopkins, Wave Theory of Aberrations. Oxford University Press, 1950.